

# Lipid Bilayers: The Effect of Force Field on Ordering and Dynamics

David Poger<sup>\*,†</sup> and Alan E. Mark<sup>†,‡</sup><sup>†</sup>The University of Queensland, School of Chemistry and Molecular Biosciences, Brisbane QLD 4072, Australia<sup>‡</sup>The University of Queensland, Institute for Molecular Bioscience, Brisbane QLD 4072, Australia

## S Supporting Information

**ABSTRACT:** The sensitivity of the structure and dynamics of a fully hydrated pure bilayer of 1,2-dipalmitoyl-*sn*-glycero-3-phosphocholine (DPPC) in molecular dynamics simulations to changes in force-field and simulation parameters has been assessed. Three related force fields (the GROMOS 54A7 force field, a GROMOS 53A6-derived parameter set and a variant of the Berger parameters) in combination with either particle-mesh Ewald (PME) or a reaction field (RF) were compared. Structural properties such as the area per lipid, carbon–deuterium order parameters, electron density profile and bilayer thicknesses, are reproduced by all the parameter sets within the uncertainty of the available experimental data. However, there are clear differences in the ordering of the glycerol backbone and choline headgroup, and the orientation of the headgroup dipole. In some cases, the degree of ordering was reminiscent of a liquid-ordered phase. It is also shown that, although the lateral diffusion of the lipids in the plane of the bilayer is often used to validate lipid force fields, because of the uncertainty in the experimental measurements and the fact that the lateral diffusion is dependent on the choice of the simulation conditions, it should not be employed as a measure of quality. Finally, the simulations show that the effect of small changes in force-field parameters on the structure and dynamics of a bilayer is more significant than the treatment of the long-range electrostatic interactions using RF or PME. Overall, the GROMOS 54A7 best reproduced the range of experimental data examined.

## 1. INTRODUCTION

Lipids are the primary building blocks of biological membranes, which act as barriers that separate the content of the cell or an organelle from its outside medium. They are also major functional components of cells alongside proteins, carbohydrates, and nucleic acids.<sup>1–3</sup> Significant functions of lipids include the regulation of vesicle trafficking by participating in the fusion, fission, budding, and reshaping of membranes and vesicles during exocytosis and endocytosis<sup>4,5</sup> and modulating the activity of membrane proteins such as ion channels<sup>6,7</sup> and G-protein-coupled receptors.<sup>8,9</sup> Understanding the structure, dynamics, and structure–function relationships of biological membranes is therefore critical. Biological membranes can be studied using various experimental techniques, including X-ray diffraction, fluorescence methods, and nuclear magnetic resonance (NMR) spectroscopy,<sup>10,11</sup> but their inherent complexity and lack of long-range order make the experimental characterization of their structure and dynamics at an atomic resolution challenging. For this reason, molecular dynamics (MD) simulation continues to be one of the primary tools used to investigate the properties of model biological membranes at an atomic or near-atomic level. The success of this approach depends upon the reliability and the accuracy of the underlying theoretical model (force field) used to describe interatomic interactions. Many alternative parameter sets have been proposed for the simulation of lipid bilayers, most of them based on the all-atom force fields CHARMM,<sup>12–16</sup> AMBER,<sup>17–19</sup> and OPLS<sup>20,21</sup> and the united-atom force field GROMOS.<sup>22–28</sup> The proliferation of alternative parameter sets for lipids has even led to the creation of the Lipidbook database, which aims to be an inventory of all published lipid force fields.<sup>29</sup>

One of the main challenges in the development of lipid force fields and an explanation for the multiplication of alternative

parameter sets is that lipids can exist in a variety of liquid-crystalline phases that vary greatly with the temperature and the level of hydration among other factors.<sup>30,31</sup> It is therefore of the utmost importance to assess each proposed force field against a broad range of available experimental properties.<sup>32</sup> The GROMOS force field has undergone continuous revision over the last three decades. Since the earliest GROMOS parameter sets developed in the mid 1980s (26C1, 37C2, and 37C4),<sup>33</sup> each successive generation of the force field has been refined so that a broader range of experimental data could be reproduced. Refinements have included the reparameterization of van der Waals interactions for nonpolar groups and the introduction of a twin-range 0.8 nm/1.4 nm cutoff scheme for both electrostatic and van der Waals interactions (GROMOS 43A1),<sup>34,35</sup> a correction of the torsion-dihedral parameters and the refinement of third-neighbor van der Waals interactions (43A2),<sup>36</sup> the reparameterization of the Lennard-Jones parameters of aliphatic carbons (43A3)<sup>37</sup> and the extension to lipids (phosphatidylcholines),<sup>38</sup> carbohydrates,<sup>39</sup> and nucleic acids<sup>40</sup> (45A4). An extensive reparameterization of nonbonded interactions involving polar groups based on the free enthalpies of hydration and apolar solvation of a range of model molecules was undertaken and led to GROMOS 53A5 and 53A6.<sup>41</sup> Most recently, the 54A7 parameter set<sup>42</sup> includes a revision of the parameters for phosphatidylcholines of varying lengths and degrees of unsaturation of the acyl tails (initially referred to as GROMOS 53A6<sub>L</sub>).<sup>28,32</sup> These latest changes have been critical for improving the application of the GROMOS force field to lipids, as earlier versions failed to reproduce the properties of a phosphatidylcholine bilayer in an L<sub>α</sub> phase appropriately.<sup>38,43,44</sup>

Received: August 1, 2012



To address this issue, several parameter sets for lipids that had been derived from the GROMOS force field have been proposed by different workers. For example, a model for 1,2-dipalmitoyl-*sn*-glycero-3-phosphocholine (DPPC) proposed by Berger et al.<sup>24</sup> has been very widely used. This model combines bonded parameters from GROMOS 37C4,<sup>22,33</sup> Lennard-Jones parameters from the united-atom OPLS force field,<sup>45</sup> and partial atomic charges from *ab initio* calculations performed by Chiu et al.<sup>23</sup> Another parameter set, derived from GROMOS 43A1 and named 43A1-S3,<sup>26</sup> focused on the optimization of torsion dihedrals and Lennard-Jones parameters for lipids through *ab initio* quantum-mechanical calculations and fitting to thermodynamic data for small reference molecules. However, such revisions—despite their popularity—result in inconsistencies when simulating mixed systems such as a membrane protein embedded in a lipid bilayer. For example, the Berger parameters are based on a 1-nm cutoff as opposed to a 1.4-nm cutoff in the GROMOS96 family of force fields (from GROMOS 43A1 on), and partially on the largely outdated GROMOS 37C4 force field. In the case of the 43A1-S3 parameter set, the optimization of van der Waals interactions in phosphatidylcholines means that atom types such as methylene groups and carbonyl carbons are described differently whether they are found in a lipid or nonlipid molecule. In an attempt to address some of these issues, Kukol<sup>27</sup> proposed a correction to the GROMOS 53A6 parameters for lipids. Specifically, Kukol suggested changing the atom type used for the carbonyl carbons in phosphatidylcholines to enhance the penetration of water into the bilayer while maintaining the consistency of the remainder of the force field.

Paradoxically, despite the rising number of membrane simulation studies, the comparison of the relative performance of different lipid force fields has been seldom documented in the literature.<sup>19,46,47</sup> Comparative studies have mostly dealt with methodological issues such as the treatment of long-range electrostatic interactions<sup>48–50</sup> or the effect of specific simulation and/or force-field parameters.<sup>48,51,52</sup> The sensitivity of various structural and dynamic properties to changes in the force field has not been examined. In this article, we present a detailed comparison of the ability of three closely related force fields to model the properties of a DPPC bilayer in the fluid phase: the native GROMOS 54A7 force field for phosphatidylcholines (originally introduced as GROMOS 53A6<sub>L</sub><sup>28</sup>), a widely used variant of the Berger parameters,<sup>48</sup> and the modification suggested by Kukol. Each of the three force fields was assessed in combination with two different schemes for the treatment of long-range electrostatic interactions: the particle-mesh Ewald (PME)<sup>53,54</sup> method and the reaction-field (RF)<sup>55</sup> method used in the parametrization of the current GROMOS force fields. We show that, while structural properties such as the area per lipid and the carbon–deuterium order parameters of the palmitoyl chains that are commonly utilized to parametrize and/or validate lipid force fields are reasonably well reproduced with all three force fields, significant differences in the ordering of the choline headgroup and the glycerol backbone and the lateral diffusion of the lipid molecules are evident. The results suggest that when using the Kukol parameters and to some extent the variant of the Berger parameters, the DPPC bilayer retained a degree of order reminiscent of a liquid-ordered phase. It is also demonstrated that the use of PME or a RF for the treatment of long-range electrostatic interactions did not influence the structural properties of the lipid bilayer significantly. Nevertheless, the treatment of long-range electrostatic interactions

did affect the dynamics of the lipid molecules. Overall, the parameters for phosphatidylcholines in the GROMOS 54A7 force field yielded the best agreement with experimental results.

## 2. METHODS

**2.1. Simulation System.** The system consisted of a preassembled lipid bilayer of 128 DPPC (1,2-dipalmitoyl-*sn*-glycero-3-phosphocholine, 16:0/16:0) molecules and 5841 water molecules (corresponding to a ratio of 45 waters per lipid) to ensure a fully hydrated state.<sup>56</sup> The bilayer was constructed by replicating a pair of lipids on an 8 × 8 grid. The area per lipid was set initially to the value of 0.640 nm<sup>2</sup> that is consistent with a DPPC bilayer in the L<sub>α</sub> phase.<sup>10</sup>

**2.2. Force-Field Parameters.** Three different force fields were tested: the GROMOS 54A7 parameter set for phosphatidylcholines<sup>28</sup> (parameter set G), the GROMOS-53A6-derived parameter set by Kukol<sup>27</sup> (parameter set K), and a widely used version of the Berger parameters<sup>24</sup> proposed by Anézo et al.<sup>48</sup> (parameter set A).

In the GROMOS 54A7 force-field parameter set, the repulsion between the choline methyls and the nonester phosphate oxygens is enhanced, in line with other highly polar groups in the GROMOS 53A6 force field.<sup>28</sup> The force-field parameters for DPPC are available as Supporting Information and in the Automated Topology Builder (ATB) and repository.<sup>57</sup> Kukol<sup>27</sup> proposed a modification of the GROMOS 53A6 force field that involved artificially enlarging the van der Waals radius of the carbonyl carbon in the glycerol backbone in order to increase the penetration of water into the lipid bilayer. This approach was similar to that initially suggested by Chandrasekhar et al. in relation to the GROMOS 45A3 force field.<sup>38</sup> Specifically, the atom type for carbonyl carbons (C) which corresponds to an sp<sup>2</sup>-hybridized carbon is replaced by the atom type CH0 normally used for bare sp<sup>3</sup> carbons. The Kukol parameters were obtained according to the Supporting Information. Both the Kukol parameters and the GROMOS 54A7 force field use the partial atomic charges proposed by Chiu et al.<sup>23</sup>

The original Berger parameters<sup>24</sup> for lipids combined bonded and nonbonded parameters from various sources: bond-stretching and valence-angle-bending terms, improper dihedrals, and dihedrals in the glycerophosphocholine moiety were taken from the GROMOS87 37C4 force field.<sup>22,33</sup> The dihedrals in the hydrocarbon chains were treated using the Ryckaert–Bellemans potential developed for liquid alkanes.<sup>58,59</sup> The Lennard-Jones parameters of the atoms were directly taken from the united-atom OPLS force field.<sup>45</sup> However, the parameters for the tails were adjusted to reproduce the density and heat of vaporisation of *n*-pentadecane. The partial atomic charges were again those suggested by Chiu et al.,<sup>23</sup> but the charge groups were modified by Berger et al. Since their original publication, multiple variations of the Berger parameters have been used in different studies. For example, the so-called Berger parameters distributed from one popular site (<http://moose.bio.ucalgary.ca>) differ from the original set proposed by Berger et al. The specific version of the Berger parameters used in this work is the same as that used by Anézo et al.<sup>48</sup> The parameters were obtained from A. H. de Vries (personal communication). This version was taken as it has been employed in multiple simulation studies of membrane systems and was used by Anézo et al. for an extensive study of the effect of different simulation conditions on the properties of a DPPC bilayer. Full details of the Anézo parameter set are given in the Supporting Information.

**Table 1. Summary of Structural Properties of an Equilibrated DPPC Bilayer Using Different Parameter Sets and Different Treatments of the Long-Range Electrostatic Interactions<sup>a</sup>**

simulation	parameter set	long-range electrostatics <sup>b</sup>	$A_L$ (nm <sup>2</sup> )	$D_{HH}$ (nm)	$D_B$ (nm)
G <sub>R</sub>	GROMOS S4A7 <sup>28</sup>	RF	0.631 (0.001)	3.53 (0.04)	3.81 (0.05)
G <sub>P</sub>	GROMOS S4A7 <sup>28</sup>	PME	0.648 (0.002)	3.51 (0.03)	3.80 (0.02)
K <sub>R</sub>	Kukol <sup>27</sup>	RF	0.626 (0.004)	3.84 (0.02)	4.05 (0.02)
K <sub>P</sub>	Kukol <sup>27</sup>	PME	0.631 (0.003)	3.72 (0.04)	3.92 (0.04)
A <sub>R</sub>	Anézo <sup>48</sup>	RF	0.629 (0.002)	3.52 (0.05)	3.82 (0.01)
A <sub>P</sub>	Anézo <sup>48</sup>	PME	0.641 (0.001)	3.62 (0.04)	3.81 (0.05)

<sup>a</sup> $A_L$ , area per lipid;  $D_{HH}$ , bilayer thickness;  $D_B$ , Luzzati bilayer thickness. The numbers between brackets are the standard deviations of the averages calculated over three simulations. <sup>b</sup>PME, particle-mesh Ewald; RF, reaction field.

**2.3. Simulation Parameters.** All simulations were performed using the GROMACS package, version 3.3.3,<sup>60</sup> under periodic boundary conditions in a rectangular box. The temperature of the system was maintained by coupling to an external temperature bath at the reference temperature of 323 K with a coupling constant of 0.1 ps using a Berendsen thermostat.<sup>61</sup> This temperature is above the gel-to-fluid phase-transition temperature of DPPC (314.4 K).<sup>62,63</sup> DPPC and water were coupled independently to the heat bath. The pressure was kept at 1 bar in the lateral and normal directions with respect to the bilayer by weakly coupling to a semi-isotropic pressure bath<sup>61</sup> using an isothermal compressibility of  $4.6 \times 10^{-5}$  bar<sup>-1</sup> and a coupling constant of 1 ps. The length of all covalent bonds within lipids were constrained using the LINCS algorithm.<sup>64</sup> The geometry of the Simple Point Charge (SPC) water molecules<sup>65</sup> was constrained using SETTLE.<sup>66</sup> The mass of the two hydrogen atoms in water was increased to 4 u (the mass of the atom of oxygen was reduced accordingly to 10 u). This allowed a 5-fs time step to be used without affecting the equilibrium properties of the system significantly.<sup>48,67</sup> Nonbonded interactions were evaluated using a twin-range cutoff scheme: interactions within the 0.8-nm short-range cutoff were calculated every step, whereas interactions within the 1.4-nm long-range cutoff were updated every 10 fs, together with the pair list. Long-range electrostatic interactions were treated using either a reaction-field (RF) correction<sup>55</sup> or the particle-mesh Ewald (PME) method.<sup>53,54</sup> In the latter case, a single cutoff of 1 nm was used for both the van der Waals and real-space terms.<sup>48,49,68</sup> In the simulations with a reaction-field correction (hereafter denoted with the subscript “R”), a relative dielectric permittivity constant of 62 was used, as appropriate for SPC water.<sup>69</sup> In the case of PME (simulations with the subscript “P”), the charges were projected onto a 0.12-nm grid using a cubic interpolation for the calculation of long-range electrostatic interactions in reciprocal space.

Each system was simulated using both a reaction field and PME. In total, six simulation setups were compared. These will be referred to as G<sub>R</sub> and G<sub>P</sub> for the systems modeled using the GROMOS S4A7 force field associated with a reaction field and PME, respectively; K<sub>R</sub> and K<sub>P</sub> when using the parameter proposed by Kukol; and A<sub>R</sub> and A<sub>P</sub> when using the Berger parameters as adapted by Anézo et al.

Each system was initially energy-minimized and then simulated at 50 K for 10 ps. The temperature was increased gradually over 100 ps until the final simulation temperature was reached. Each system was simulated three times with different initial atomic velocities. The equilibration of the systems was monitored by examining the time evolution of the potential energy and the area per lipid of the system. Once the systems had reached equilibrium, data were collected for 200 ns (the

details of the methodology used to verify that the systems were at equilibrium when the simulations were analyzed are provided as Supporting Information). Analysis was performed on each of the three simulations for each system and then averaged.

### 3. RESULTS AND DISCUSSION

In the following section, the structure and the dynamics of the DPPC bilayer are discussed. In particular, the ordering of the glycerophosphocholine group is examined. The NMR-derived quadrupolar splitting in the choline and glycerol moieties is calculated and compared to experimental results. The radial distribution function of the carbonyl carbons in the plane of the bilayer is also analyzed.

**3.1. Structure of the Bilayer.** The structure of the DPPC bilayers resulting from the different simulations were compared based on the area per lipid ( $A_L$ ), the electron density profile, the thicknesses  $D_{HH}$  and  $D_B$ , the ordering of the lipids (carbon–deuterium order parameters and quadrupolar splitting), the two-dimensional radial distribution function of the carbonyl carbons in glycerol, and the relative orientation of the headgroup dipole.

**3.1.1. Area per lipid.** The area per lipid  $A_L$  was calculated as the lateral area of the simulation box divided by the number of lipids in each leaflet. All the values of  $A_L$  listed in Table 1 are within 3% of each other. All are in general agreement with recent estimates of the area per lipid of DPPC in a  $L_\alpha$  phase (0.628 nm<sup>2</sup>,<sup>70</sup> 0.629 nm<sup>2</sup>,<sup>56</sup> 0.631 nm<sup>2</sup>,<sup>70</sup> 0.633 nm<sup>2</sup>,<sup>71</sup> 0.64 nm<sup>2</sup>,<sup>10</sup> 0.642 nm<sup>2</sup>,<sup>72</sup>). Although  $A_L$  is often used to assess the validity of force fields and the convergence of simulations, it appears relatively insensitive to the nature of the force field and the method used to treat long-range electrostatics (RF or PME).<sup>32,48</sup>

**3.1.2. Electron Density Profiles.** The electron density profiles derived from the simulations using a reaction-field correction (simulations G<sub>R</sub>, K<sub>R</sub>, and A<sub>R</sub>) or PME (simulations G<sub>P</sub>, K<sub>P</sub>, and A<sub>P</sub>) are shown in Figures 1 and 2, respectively. The profiles were calculated by dividing the simulation box into 100 slices along the normal to the bilayer ( $z$  axis). The partial density for every atom in each slice was weighted by its number of electrons and averaged over the simulation. The total electron density profiles of the hydrated DPPC bilayers are presented in panels A of Figures 1 and 2, together with the electron density profiles for water only. The two peaks in the total electron density profiles correspond to the headgroups. A decomposition of the total electron densities into the contributions from different components in DPPC is shown in panels B (choline, Cho, and phosphate, P), C (glycerol backbone, Gro, and *sn*-1 and *sn*-2 carbonyls, CO), and D (methylenes, CH<sub>2</sub>, and terminal methyls, CH<sub>3</sub>, of the palmitoyl chains) of Figures 1 and 2. The profiles are symmetric,



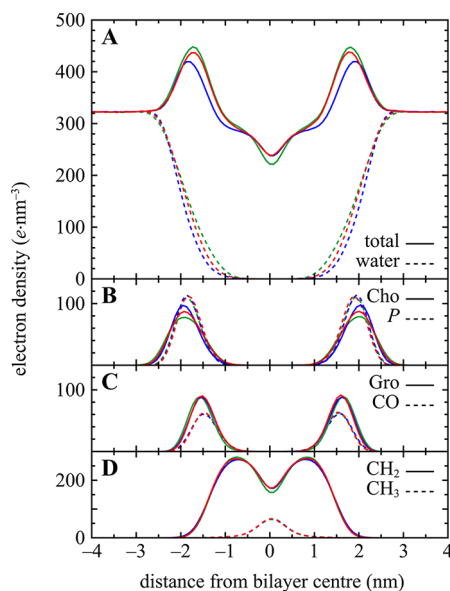


**Figure 1.** Average electron density profiles of the hydrated DPPC bilayer from simulations  $G_R$  (black),  $K_R$  (blue), and  $A_R$  (green). (A) Electron density profiles of the whole system and water. (B–D) Contribution of the individual components of the bilayer: (B) choline (Cho) and phosphate (P) groups; (C) glycerol (Gro) and carbonyls (CO); (D) methylene ( $CH_2$ ) and terminal methyl ( $CH_3$ ) groups of the palmitoyl chains.

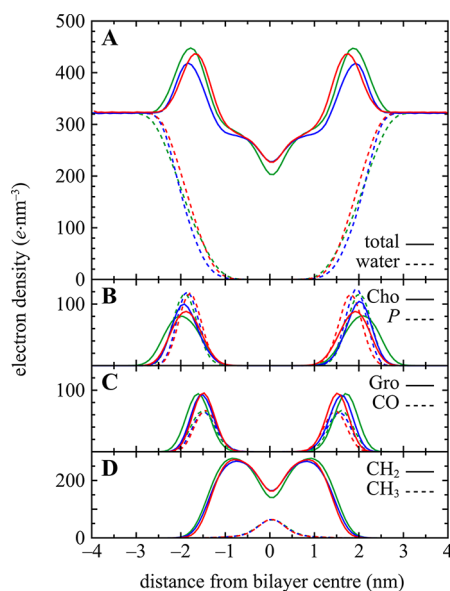


**Figure 2.** Average electron density profiles of the hydrated DPPC bilayer from simulations  $G_P$  (black),  $K_P$  (blue), and  $A_P$  (green). (A) Electron density profiles of the whole system and water. (B–D) Contribution of the individual components of the bilayer: (B) choline (Cho) and phosphate (P) groups; (C) glycerol (Gro) and carbonyls (CO); (D) methylene ( $CH_2$ ) and terminal methyl ( $CH_3$ ) groups of the palmitoyl chains.

indicating that the bilayers are well equilibrated. The nature of the force field and the method used to treat the long-range electrostatics primarily affect the position and the intensity of the density in the headgroup region. When using a reaction field (Figure 1A), the total density profiles are almost identical for  $G_R$  and  $A_R$ . In the case of  $K_R$ , the peaks are less intense and separated by a greater distance than those from simulations  $G_R$

and  $A_R$ . This is mostly due to a lower penetration of water into the headgroup regions (Figure 1A) and a larger distance between the two mean choline planes in the bilayer (Figure 1B). Using PME, there are distinct differences in the electron density profiles of the headgroup and glycerol regions between the three simulations (Figure 2). These are caused in part by differences in the penetration of water into the bilayer (Figure 2A) but also in the distribution of the choline (Figure 2B), phosphate (Figure 2B), glycerol (Figure 2C), and carbonyl groups (Figure 2C). Note, the dip in the density at the center of the bilayer in Figures 1A and 2A is also consistently lower when using the An  zo parameter set (simulations  $A_R$  and  $A_P$ , respectively). Panels D in Figures 1 and 2 suggest that this is caused by a greater segregation of the  $CH_2$  groups in the palmitoyl chains between the two leaflets. This may be due to an enhanced repulsion in the Lennard-Jones potential in the An  zo parameters than in the GROMOS 53A6/54A7 force field (for example for  $CH_3$  groups in acyl chains,  $\sigma$  is 0.396 and 0.375 nm, respectively, in combination with a cutoff of 1.4 nm).

The density profiles computed from the simulations can be compared with those obtained experimentally from X-ray scattering measurements. The distance  $D_{HH}$  between the two peaks of the total electron density profile is commonly referred to as the bilayer thickness. The Luzzati thickness  $D_B^{10,30}$  can also be computed using

$$D_B = b_z - \int_0^{b_z} \rho_w(z) dz \quad (1)$$

where  $b_z$  is the dimension of the simulation box along the  $z$  axis (normal to the bilayer) and  $\rho_w(z)$  is the probability distribution of water along  $z$ .  $\rho_w(z)$  was determined from the time-averaged histogram of the distribution of water along the  $z$  axis with a bin width of  $\Delta z$ :

$$\rho_w(z) = \frac{n_w(z)V_w}{\Delta V} \quad (2)$$

where  $n_w(z)$  is the time-averaged number of water molecules per slice of thickness  $\Delta z$ ,  $\Delta V$  is the time-averaged volume of a slice, and  $V_w$  is the volume per water molecule. It was previously determined that  $V_w = 3.15 \times 10^{-2} \text{ nm}^3$  for a SPC molecule at 323 K and at a pressure of 1 bar.<sup>28</sup>  $D_{HH}$  and  $D_B$  vary with the phase of the bilayer: a DPPC bilayer is thicker in a gel ( $L_{\beta'}$ ) phase (experimentally,  $D_{HH} = 4.50 \text{ nm}$  and  $D_B = 4.98 \text{ nm}$ )<sup>73</sup> than in the  $L_\alpha$  phase (experimental values of  $D_{HH}$ : 3.42 nm,<sup>74</sup> 3.64 nm,<sup>56</sup> 3.78 nm,<sup>72</sup> 3.80 nm,<sup>70</sup> and 3.83 nm<sup>10</sup> and  $D_B$ : 3.85 nm,<sup>10</sup> 3.90 nm,<sup>70</sup> and 3.92 nm<sup>56</sup>). The values of  $D_{HH}$  and  $D_B$  calculated from the simulations are listed in Table 1. In all cases, the values of  $D_{HH}$  lie within 5% of the range of the values determined experimentally. The values of  $D_B$  calculated from the simulations fall within 2–4% of the experimental values. The values of both  $D_{HH}$  and  $D_B$  obtained in the simulations  $G_R$ ,  $G_P$ ,  $A_R$ , and  $A_P$  lie toward the lower range of the experimental values, while the values for  $K_R$  and  $K_P$  are toward the upper range of the experimental values. Again, no significant difference is evident between the three force fields nor between PME and RF

**3.1.3. Order Parameters.** An indication of the degree of structure and ordering within the lipids in the bilayer can be obtained experimentally using  $^2\text{H}$  NMR spectroscopy through the determination of a carbon–deuterium order parameter  $S_{CD}$ . The  $S_{CD}$  of the two methylene groups in the choline headgroup at positions  $\alpha$  and  $\beta$ , the two methylenes and the methanetriyl

group at positions *sn*-1, *sn*-3, and *sn*-2, respectively, in the glycerol backbone, and the methylene groups in the *sn*-2 palmitoyl chain was calculated and compared to experimental data, when available. The positions  $\alpha$ ,  $\beta$ , *sn*-1, *sn*-2, and *sn*-3 in DPPC are illustrated in Figure 3.  $S_{CD}$  measures the relative

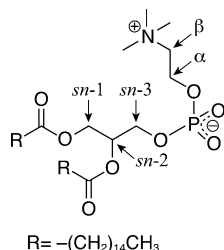


**Figure 3.** Structure and naming convention used for the methylene ( $CH_2$ ) and methanetriyl ( $CH$ ) groups in DPPC.

orientation of the C–D bonds with respect to the bilayer normal. The order parameter  $S_{CD}$  of a group is defined as

$$S_{CD} = \frac{1}{2} \langle 3 \cos^2 \theta - 1 \rangle \quad (3)$$

where  $\theta$  is the angle between a C–D bond of the methylene or methanetriyl group and the normal to the bilayer (taken as the  $z$  axis). The angular brackets denote an average over all the lipids and the simulation. As GROMOS 54A7 is a united-atom force field wherein aliphatic hydrogens are treated implicitly and incorporated into the carbon to which they are bound, the positions of the deuterons were constructed on the basis of the positions of the neighboring heavy atoms assuming tetrahedral geometry. The  $|S_{CD}|$  profiles of the *sn*-2 palmitoyl chain of DPPC from the simulations together with the experimental profiles determined by NMR by Douliez et al.<sup>75</sup> and Petrache et al.<sup>71</sup> are presented in Figure 4. Note the carbons are numbered from the carbonyl group of the palmitoyl chain. The  $|S_{CD}|$  values calculated from each of the simulations reproduce the overall trends in the experimental data well. In general, the simulations performed using a RF ( $G_R$ ,  $K_R$ , and  $A_R$ ; Figure 4A) yielded  $|S_{CD}|$  values 0.01–0.02 higher than the simulations using PME ( $G_P$ ,  $K_P$ , and  $A_P$ ; Figure 4B). The lowest and highest  $|S_{CD}|$  values were computed from simulations  $G_P$  and  $K_R$ , respectively. Nonetheless, the variation between the two sets of simulations is in the same range as the variation between the two sets of experimental data. There is some discrepancy between the values proposed by Douliez et al.<sup>75</sup> and Petrache et al.<sup>71</sup> for the first methylene (at position 2) and the values obtained in all the simulations. However, Douliez et al.<sup>75</sup> reported that the  $|S_{CD}|$  value for the first methylene could be difficult to determine accurately, partly because of the existence of a local conformational equilibrium.<sup>76,77</sup>

The ordering of the choline headgroup and glycerol backbone in the simulations was compared to experimental results by calculating the quadrupolar splitting  $|\Delta\nu_Q|$ . The quadrupolar splittings  $\Delta\nu_\alpha$ ,  $\Delta\nu_\beta$ ,  $\Delta\nu_1$ ,  $\Delta\nu_2$ , and  $\Delta\nu_3$  for the deuterons at positions  $\alpha$ ,  $\beta$ , *sn*-1, *sn*-2, and *sn*-3, respectively, were derived from the corresponding values of the  $S_{CD}$  using

$$|\Delta\nu_Q| = \frac{3}{4} \frac{e^2 q Q}{h} |S_{CD}| \quad (4)$$

where  $e^2 q Q/h = 167$  kHz is the static quadrupole splitting constant of D in C–D bonds.<sup>78</sup> The values of  $|\Delta\nu_Q|$  for the

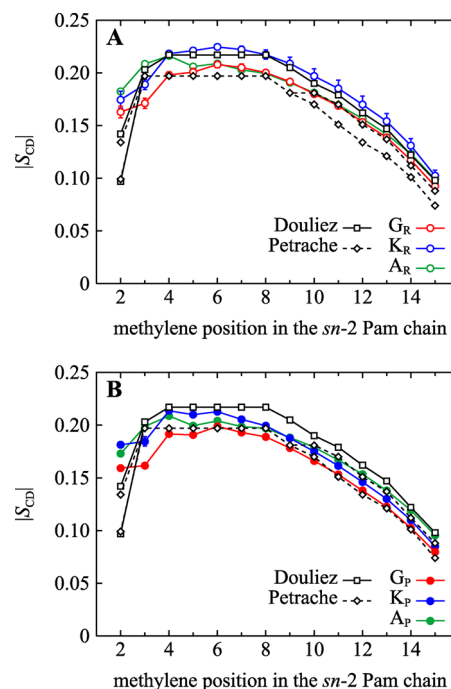


**Figure 4.** Deuterium order parameter  $|S_{CD}|$  profiles of the *sn*-2 palmitoyl (Pam) chain of DPPC in simulations using (A) a reaction-field correction ( $G_R$ ,  $K_R$ , and  $A_R$ ), and (B) particle-mesh Ewald ( $G_P$ ,  $K_P$ , and  $A_P$ ) for the treatment of long-range electrostatics. The  $|S_{CD}|$  values are averaged over all the lipid *sn*-2 palmitoyl chains in the bilayer and over three simulations. Errors bars are mostly within the size of the symbols. Experimental  $|S_{CD}|$  values of Douliez et al.<sup>75</sup> ( $\square$ ) and Petrache et al.<sup>71</sup> ( $\diamond$ ) are also shown. The two values of  $|S_{CD}|$  measured by Douliez et al. and Petrache et al. at position 2 correspond to the *pro*-R and *pro*-S deuterons. Note, data for carbons 3–15 from Petrache et al. are given for the *sn*-1 and *sn*-2 chains as the authors did not differentiate them.

methylenes in choline and the methylenes and methanetriyl in glycerol are listed in Table 2. The values of  $|\Delta\nu_Q|$  of the  $\alpha$ - and  $\beta$ -methylenes calculated from the simulations differ significantly depending on the parameter set. Experimentally, for a DPPC bilayer in the fluid phase,  $|\Delta\nu_\alpha|$  and  $|\Delta\nu_\beta|$  are close to 5 kHz (5.8 kHz,<sup>79</sup> 5.9 kHz,<sup>80</sup> 5.95 kHz,<sup>81</sup> and 6 kHz<sup>82</sup> at position  $\alpha$ ; 3.2 kHz,<sup>79</sup> 4.81 kHz,<sup>81</sup> 5.1 kHz,<sup>80</sup> and 5.3 kHz<sup>82</sup> at position  $\beta$ ). The ordering of the C–D bonds at the  $\alpha$  position is best captured using GROMOS 54A7 ( $G_R$  and  $G_P$ ).  $|\Delta\nu_\alpha|$  ranges from 0.7 kHz in the case of simulation  $A_P$  to 17.1 kHz for  $K_R$ . Likewise, the values of  $|\Delta\nu_\beta|$  range from 2.1 kHz for  $G_P$  to 7.8 kHz for  $A_P$ . Experimentally, it is found that the  $\beta$ -methylene in choline has a comparable or lower degree of ordering than the  $\alpha$ -methylene. Only the simulations using the GROMOS 54A7 and Kukol parameter sets reproduced this aspect. Interestingly, the Anézo parameter set shows the opposite trend with the  $\alpha$ -methylene being markedly more disordered than the  $\beta$ -methylene. The value of  $|\Delta\nu_\beta|$  from simulation  $A_P$  is also relatively close to that measured in a phosphatidylcholine bilayer in a gel phase (about 8 kHz).<sup>82,83</sup>

The ordering of glycerol also varies between the parameter sets. The quadrupolar splittings at positions *sn*-2 (26.1 kHz<sup>84</sup>) and *sn*-3 (28 kHz on average<sup>80</sup>) have been determined experimentally for phosphatidylcholines. The quadrupolar splitting at position *sn*-1 (about 8.5 kHz on average<sup>85</sup>) was measured on labeled phosphatidylglycerols and phosphatidylethanolamines but was shown to be also valid for phosphati-

**Table 2.** Quadrupolar Splitting of the Methylene and Methanetriyl Groups in the Choline Headgroup at the  $\alpha$  ( $|\Delta\nu_\alpha|$ ) and  $\beta$  ( $|\Delta\nu_\beta|$ ) Positions and in Glycerol at the *sn*-1 ( $|\Delta\nu_1|$ ), *sn*-2 ( $|\Delta\nu_2|$ ) and *sn*-3 ( $|\Delta\nu_3|$ ) Positions in DPPC Molecules Calculated in the Simulations<sup>a</sup>

simulation	choline		glycerol		
	$ \Delta\nu_\alpha $ (kHz)	$ \Delta\nu_\beta $ (kHz)	$ \Delta\nu_1 $ (kHz)	$ \Delta\nu_2 $ (kHz)	$ \Delta\nu_3 $ (kHz)
G <sub>R</sub>	10.8 (0.4)	2.2 (0.1)	2.5 (0.5)	21.9 (1.8)	19.1 (0.7)
G <sub>P</sub>	10.4 (0.4)	2.1 (0.2)	7.7 (0.1)	20.8 (0.4)	20.3 (0.1)
K <sub>R</sub>	17.1 (0.7)	2.3 (0.3)	6.7 (1.1)	45.4 (0.3)	24.6 (1.1)
K <sub>P</sub>	17.0 (0.1)	3.2 (0.7)	10.9 (0.4)	42.8 (0.7)	26.3 (0.3)
A <sub>R</sub>	1.5 (0.3)	5.9 (0.2)	22.7 (0.2)	21.8 (0.8)	12.7 (0.3)
A <sub>P</sub>	0.7 (0.4)	7.8 (0.4)	24.1 (0.3)	15.4 (1.1)	13.4 (0.7)

<sup>a</sup>The numbers between brackets are the standard deviations of the averages calculated over three simulations.

dylcholines. Note, the two deuterons in each of the two methylene groups at the *sn*-1 and *sn*-3 positions are enantiotopic, so they exhibit different quadrupolar splittings in <sup>2</sup>H NMR experiments (0 kHz and about 17 kHz at position *sn*-1;<sup>85</sup> 27 kHz and 29 kHz at position *sn*-3<sup>78,82</sup>). The ordering of the deuterons at position *sn*-1 is best reproduced with the Kukol parameter set with values of  $|\Delta\nu_1|$  of 6.7 kHz and 10.9 kHz for simulations K<sub>R</sub> and K<sub>P</sub>, respectively, and to a reasonable extent with the GROMOS 54A7 force field with values of 2.5 kHz and 7.7 kHz for simulations G<sub>R</sub> and G<sub>P</sub>, respectively. In contrast, the Anézo parameter set tends to markedly enhance local ordering ( $|\Delta\nu_1| \approx 23$  kHz). The calculated splittings at positions *sn*-2 and *sn*-3 are in best agreement with the experimental values when using the GROMOS 54A7 force field ( $|\Delta\nu_Q| \approx 19$ –22 kHz). With the Kukol parameter set, the *sn*-2 methanetriyl is more ordered than the *sn*-3 methylene ( $|\Delta\nu_2| \approx 44$  kHz and  $|\Delta\nu_3| \approx 25$  kHz). The Anézo parameters globally lead to less restricted motions of the *sn*-2 and *sn*-3 groups ( $|\Delta\nu_2|$  and  $|\Delta\nu_3|$  are about 50% lower than their respective experimental values).

**3.1.4. Ordering of the Carbonyls.** In order to further assess differences in the degree of ordering induced by the three parameter sets in the polar region of the DPPC bilayer, the two-dimensional radial distribution function (RDF)  $g(r)$  of the *sn*-1 and *sn*-2 carbonyl carbons in each leaflet of the bilayer was obtained using

$$g(r) = \frac{n(r)}{2\pi r \Delta r \bar{\rho}} \quad (5)$$

where  $n(r)$  is the time-averaged number of carbonyl carbons at a distance between  $r$  and  $r + \Delta r$  around another carbonyl carbon within the same leaflet of the bilayer and  $\bar{\rho}$  is the time-averaged density of carbonyl carbons in the same leaflet within 4 nm of a central carbonyl carbon (taking the periodic boundary conditions into account).  $\bar{\rho}$  was averaged over the two leaflets of the bilayer. The RDFs calculated for each of the simulations are given in Figure 5. The inset in Figure 5 shows the equivalent RDF obtained from the simulation of a liquid-ordered (*L*<sub>o</sub>) DPPC bilayer using the GROMOS 53A6 parameters (including the GROMOS96 partial atomic charges).<sup>28</sup> It was shown previously that this parameter set leads to a highly ordered, gel-like DPPC bilayer.<sup>28</sup> It is clear from Figure 5 that while the RDF is influenced strongly by the nature of the force field used, it is virtually unaffected whether PME or RF is employed for the treatment of long-range electrostatics. From Figure 5, it can be seen that, using the GROMOS 54A7 (G<sub>R</sub> and G<sub>P</sub>) and the Anézo parameters (A<sub>R</sub> and A<sub>P</sub>), there is almost no structure beyond the second shell of neighbors lying at about

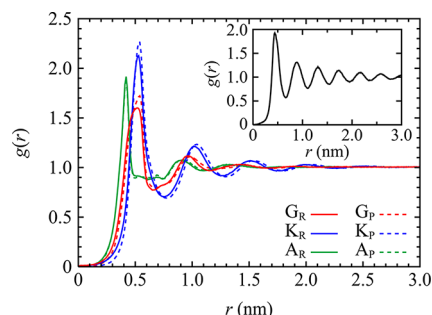


**Figure 5.** Average two-dimensional radial distribution function  $g(r)$  of the distance between the carbonyl carbons of the same leaflet in a DPPC bilayer in simulations G<sub>R</sub>, G<sub>P</sub>, K<sub>R</sub>, K<sub>P</sub>, A<sub>R</sub>, and A<sub>P</sub>. Inset:  $g(r)$  calculated from the simulation of a DPPC bilayer in a liquid-ordered (*L*<sub>o</sub>) phase.

1.1 nm in simulations G<sub>R</sub> and G<sub>P</sub> and 1 nm in simulations A<sub>R</sub> and A<sub>P</sub>, from the central carbon atom. In contrast, the RDFs from simulations K<sub>R</sub> and K<sub>P</sub> show a high degree of ordering of the carbonyl carbons up to about 1.5–2 nm from the central atom with three well-defined shells of neighbors. In fact, the RDFs are reminiscent of that of a DPPC bilayer in an *L*<sub>o</sub> phase, suggesting that, despite the lack of experimental data to compare the distribution of carbonyl carbons against, the two-dimensional distribution of the carbonyl carbons is halfway between an ordered, gel-like state and a disordered, fluid state. The first shell of neighbors (at 0.52 nm, 0.54 nm, 0.53 nm, 0.53 nm, 0.42 nm, and 0.42 nm in simulations G<sub>R</sub>, G<sub>P</sub>, K<sub>R</sub>, K<sub>P</sub>, A<sub>R</sub>, and A<sub>P</sub>, respectively) includes among others the *sn*-1 and *sn*-2 carbonyl carbons of the same lipid molecules. The corresponding peak is significantly sharper and about 0.1 nm closer to the central atom in simulations A<sub>R</sub> and A<sub>P</sub> than in the other simulations, indicating that the Anézo parameter set yields higher short-range ordering than the GROMOS 54A7 and Kukol parameter sets.

**3.1.5. Orientation of the Headgroups.** The tilt of the headgroups was characterized by calculating the angle  $\zeta$  between the P→N dipole moment vector that connects the phosphorus and the nitrogen atoms in the phosphocholine headgroup and the outward bilayer normal (pointing away from the core of the bilayer). Experimentally, Büldt et al.<sup>86</sup> showed that the P→N dipole lies almost parallel to the plane of the bilayer. The probability distribution of  $\zeta$  calculated from the simulations together with that from the DPPC bilayer in an *L*<sub>o</sub> phase are displayed in Figure 6. The most probable values of  $\zeta$  were 82°, 76°, 78°, 78°, 93°, and 78° for simulations G<sub>R</sub>, G<sub>P</sub>, K<sub>R</sub>, K<sub>P</sub>, A<sub>R</sub>, and A<sub>P</sub>, respectively. Thus, the headgroups are mostly oriented parallel to the surface of the bilayer. However,



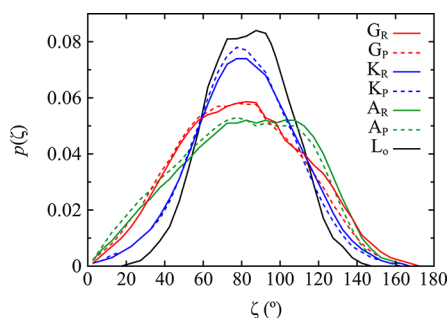


**Figure 6.** Average probability distribution of the angle  $\zeta$  between the bilayer normal pointing away from the bilayer to bulk water and the lipid headgroup P→N dipole moment vector in simulations  $G_R$ ,  $G_P$ ,  $K_R$ ,  $K_P$ ,  $A_R$ ,  $A_P$  and in the simulation of a DPPC bilayer in a liquid-ordered ( $L_o$ ) phase.

the shape of the distributions of  $\zeta$  varies. It is a relatively broad, parabolic-shaped peak in simulations  $G_R$ ,  $G_P$ ,  $A_R$  and  $A_P$ , indicating a high degree of disorder in the headgroup region. In contrast, the distributions obtained from simulations  $K_R$  and  $K_P$  are more Gaussian in nature with a well-defined peak, suggesting a higher degree of ordering, much closer to that observed in the simulation of a liquid-ordered bilayer and shown in Figure 6.

**3.2. Lipid Dynamics.** The lateral diffusion coefficient  $D_{xy}$  of a lipid in the plane of the bilayer (i.e., in the  $xy$  plane) was calculated using the Einstein relation

$$D_{xy} = \frac{1}{2n_f} \lim_{t \rightarrow \infty} \frac{1}{t} \langle \|\mathbf{r}_{xy}(t + t_0) - \mathbf{r}_{xy}(t_0)\|^2 \rangle_{t_0} \quad (6)$$

where  $n_f$  is the number of translational degrees of freedom ( $n_f = 2$ ) and  $\mathbf{r}_{xy}(t)$  is the lateral position of the center of mass of a lipid molecule at time  $t$ .  $\langle \|\mathbf{r}_{xy}(t + t_0) - \mathbf{r}_{xy}(t_0)\|^2 \rangle_{t_0}$  is the lateral mean square displacement (MSD) of a lipid over  $t$  calculated over all possible starting times  $t_0 < t$ . In practice,  $D_{xy}$  was derived from the slope of the time evolution of the MSD of the center of mass of each DPPC molecule projected onto the  $xy$  plane. The slope was estimated over the time interval  $20 \text{ ns} \leq t \leq \tau$ , during which the variation of the MSD was linear with time for all simulations,  $\tau$  ranging from 150 to 200 ns depending on the simulation. The lateral diffusion coefficient  $D_{xy}$  was obtained by averaging the MSD over all of the 128 DPPC molecules in the bilayer with  $20 \text{ ns} \leq t_0 \leq \tau$ . The evolution of the MSD as a function of the averaging time calculated for each of the simulations is given in Figure 7. It can

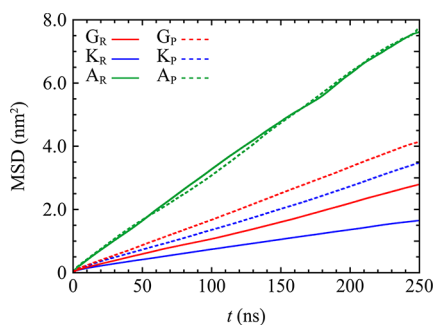


**Figure 7.** Evolution of the mean square displacement (MSD) of the center of mass of the lipid molecules as a function of the averaging time  $t$  in simulations  $G_R$ ,  $G_P$ ,  $K_R$ ,  $K_P$ ,  $A_R$ , and  $A_P$ .

be seen that the MSD varies linearly with time until an averaging time of 150–200 ns. The value of  $D_{xy}$  can therefore be determined from the slope of the evolution of the MSD in this region.

Similarly, the linear diffusion coefficients of the DPPC molecules along the  $x$  and  $y$  axes ( $D_x$  and  $D_y$ , respectively) were calculated using the following equation:

$$D_\alpha = \frac{1}{2n_f} \lim_{t \rightarrow \infty} \frac{1}{t} \langle \|\mathbf{r}_\alpha(t + t_0) - \mathbf{r}_\alpha(t_0)\|^2 \rangle \quad (7)$$

with  $n_f = 1$  and  $\alpha = x$  or  $y$ . The lateral and linear MSDs of the lipids, from which  $D_{xy}$  and  $D_x$  and  $D_y$  were respectively derived, were corrected for the motions of the center of mass of each leaflet at each step. The values of  $D_x$ ,  $D_y$ , and  $D_{xy}$  obtained from the simulations are given in Table 3. The values obtained for

**Table 3. Linear and Lateral Diffusion Coefficients of DPPC Molecules Calculated in the Simulations<sup>a</sup>**

simulation	$D_x$ ( $10^{-8} \text{ cm}^2 \text{ s}^{-1}$ )	$D_y$ ( $10^{-8} \text{ cm}^2 \text{ s}^{-1}$ )	$D_{xy}$ ( $10^{-8} \text{ cm}^2 \text{ s}^{-1}$ )
$G_R$	2.6 (0.2)	2.3 (0.1)	2.6 (0.2)
$G_P$	4.3 (0.2)	3.9 (0.3)	4.1 (0.3)
$K_R$	1.7 (0.1)	1.8 (0.1)	1.7 (0.1)
$K_P$	3.0 (0.3)	2.9 (0.4)	3.0 (0.3)
$A_R$	7.2 (0.5)	7.3 (0.7)	7.4 (0.4)
$A_P$	9.1 (0.4)	8.8 (1.1)	9.1 (0.1)

<sup>a</sup> $D_x$ , linear diffusion coefficient along the  $x$  axis;  $D_y$ , linear diffusion coefficient along the  $y$  axis;  $D_{xy}$ , lateral diffusion coefficient. The numbers between brackets are the standard deviations of the averages calculated over three simulations.

the lateral ( $D_{xy}$ ) and linear ( $D_x$  and  $D_y$ ) diffusion coefficients are similar in all simulations, demonstrating that the DPPC molecules moved freely and isotropically in the plane of the bilayer. Overall, it was found that the GROMOS 54A7 and Kukol parameter sets led to values of  $D_{xy}$  around  $2\text{--}4 \times 10^{-8} \text{ cm}^2 \text{ s}^{-1}$ , whereas  $D_{xy}$  was  $7.4 \times 10^{-8} \text{ cm}^2 \text{ s}^{-1}$  and  $9.1 \times 10^{-8} \text{ cm}^2 \text{ s}^{-1}$  in simulations  $A_R$  and  $A_P$ , respectively, with the Anézo parameter set. Interestingly, the diffusion coefficients were systematically 20–40% lower when using a reaction-field correction as opposed to PME. The values of  $D_{xy}$  are in general similar to those obtained for DOPC with the force field GAFF and the Berger parameters by Siu et al.<sup>19</sup> but lower than in other simulation studies of a fluid DPPC bilayer using the parameters by or derived from the work by Berger et al. where the lateral diffusion coefficient was often estimated around  $7\text{--}13 \times 10^{-8} \text{ cm}^2 \text{ s}^{-1}$ .<sup>20,48,50,87</sup> These differences could either be a result of the modifications of the original Berger parameters introduced by Anézo and others or differences in simulation conditions. For example, using too low a frequency for updating the nonbonded pair list can lead to spurious forces which will artificially enhance the diffusion of lipids. In their simulations using the GROMOS 43A1 force field, Bonvin et al.<sup>88</sup> noticed that the reorientation of water became a major source of heating of the system when the nonbonded pair list was update every 20 fs or more. They found that, to avoid spurious heating, the maximum delay between pair-list updates was 10 fs. In the studies aforementioned,<sup>48,50,87</sup> the nonbonded interactions and the pair list were updated every 20 fs; it is then possible that the higher values of  $D_{xy}$  measured by the authors whether they used PME or RF are partly artifactual. The difference between the use of PME and the reaction-field correction could also result from the difference in the calculation of the long-range van der

Waals interactions. When using PME, a single cutoff of 1 nm was used for both the Lennard-Jones interactions and the real-space part of the electrostatics, whereas a long-range cutoff of 1.4 nm was used for electrostatic and Lennard-Jones interactions when using the reaction-field approach. While the use of PME will have slightly enhanced the electrostatic interaction, this will be offset by the decrease in the attractive part of the Lennard-Jones interactions, which could explain in part the higher diffusion coefficients calculated for simulations  $G_P$  and  $K_P$  with respect to simulations  $G_R$  and  $K_R$ , respectively. The use of heavy hydrogen atoms in the water may also have contributed to the difference with other simulation studies.

Experimentally, the lateral diffusion of lipids along the bilayer plane has been studied using various methods including fluorescence techniques—such as fluorescence recovery after photobleaching (FRAP),<sup>89,90</sup> Förster resonance energy transfer (FRET),<sup>91</sup> excimer formation,<sup>92,93</sup> fluorescence correlation spectroscopy (FCS),<sup>94–96</sup> single-particle tracking (SPT),<sup>97,98</sup> and continuous fluorescence microphotolysis (CFM)<sup>99</sup>—quasi-elastic neutron scattering (QENS),<sup>100–103</sup> electron paramagnetic resonance spectroscopy,<sup>104,105</sup> electrochemical impedance spectroscopy,<sup>106,107</sup> and various NMR techniques—including  $^1\text{H}$ ,  $^2\text{H}$ ,  $^{19}\text{F}$ , and  $^{31}\text{P}$  NMR.<sup>108–117</sup> A list of experimental values of  $D_{xy}$  measured in a DPPC bilayer in the fluid phase together with the types of method used is given in Table 4. The degree of variation is striking. The values of  $D_{xy}$  range over 3 orders of magnitude from  $0.22 \times 10^{-8} \text{ cm}^2 \cdot \text{s}^{-1}$ <sup>108</sup> to  $460 \times 10^{-8} \text{ cm}^2 \cdot \text{s}^{-1}$ .<sup>101</sup> This variation is not only between techniques but also between different studies using the same method. For example, Scomparin et al.<sup>90</sup> estimated the lateral diffusivity of DPPC in a fluid-phase bilayer with FRAP using two closely related lipid probes derived from the fluorophore NBD (7-nitro-2,1,3-benzoxadiazole): a NBD-bound phosphatidylcholine (NBD-PC(16:0/12:0)) and a NBD-bound phosphatidylethanolamine (NBD-DPPE). They found that  $D_{xy}$  could change by 1 order of magnitude depending on the nature of the probe and whether the sample was a supported single or double bilayer. The values of  $D_{xy}$  obtained by  $^1\text{H}$ ,  $^2\text{H}$ , and  $^{31}\text{P}$  NMR listed in Table 4 also range from  $0.22 \times 10^{-8} \text{ cm}^2 \cdot \text{s}^{-1}$ <sup>108</sup> to  $30 \times 10^{-8} \text{ cm}^2 \cdot \text{s}^{-1}$ .<sup>111</sup> The reason for the variation observed in Table 4 is multiple: (i) The lateral diffusion of lipids in bilayers is sensitive to experimental conditions such as temperature,<sup>90,118</sup> pressure,<sup>119</sup> hydration content,<sup>102,120</sup>  $\text{pH}$ ,<sup>107</sup> ionic strength,<sup>107</sup> composition of the bilayer,<sup>106,117,120</sup> and experimental setup.<sup>90,95</sup> (ii) The lateral diffusion of lipids within the plane of a bilayer is inferred from models which themselves contain a number of assumptions. For example, in FRAP,  $D_{xy}$  can be deduced from the rate of the fluorescence recovery using various models, all of them relying on the Stokes–Einstein relationship that approximates diffusing particles as spheres.<sup>121</sup> (iii) EPR, NMR, and fluorescence techniques measure motions over distances ( $>0.1 \text{ m}$ ) and time scales (ns–ms) which are longer than those sampled by neutron scattering experiments (0.1–10 nm and  $<1 \text{ ns}$ ). As a result, neutron scattering is sensitive to fast, short-range diffusion (cage diffusion,  $D_{xy} \approx (10\text{--}100) \times 10^{-8} \text{ cm}^2 \cdot \text{s}^{-1}$ ), whereas EPR, NMR, and fluorescence methods generally sample slower, medium-to-long-range diffusion processes (random-walk diffusion,  $D_{xy} \approx (1\text{--}10) \times 10^{-8} \text{ cm}^2 \cdot \text{s}^{-1}$ ).<sup>122</sup> Although computer simulations can probe both types of diffusion, the diffusion coefficient calculated here corresponds to the slow-diffusion regime. (iv) Some techniques, in particular EPR and fluorescence methods, require labels (spin labels or fluorescence dyes). In this case,

**Table 4.** Summary of some Lateral Diffusion Coefficients ( $D_{xy}$ ) Measured Experimentally in Fluid-Phase DPPC Bilayer<sup>a</sup>

method <sup>b</sup>	nature of the probe <sup>c</sup>	temperature (K)	$D_{xy} (10^{-8} \text{ cm}^2 \cdot \text{s}^{-1})$
fluorescence spectroscopy			
triplet–triplet annihilation	APE	323	$23^{127}$
FRAP	diOC <sub>18</sub> (3)	318	$7^{128}$
excimer fluorescence	PPDPC	323	$16^{92}$
excimer fluorescence	PDA	323	$26^{92}$
excimer fluorescence	pyrene	323	$40^{92}$
FRAP	NBD-DPPE	323	$12^{89}$
excimer fluorescence	pyrene	323	$48\text{--}224^{118}$
FCS	rhodamine Red-X DHPE	$296^d$	$18^{95}$
FRAP	NBD-DPPE	318–319	$1.7\text{--}3.2^{90}$
FRAP	NBD-PC (16:0/12:0)	323	$14^{90}$
magnetic spectroscopy			
EPR	ASL	323	$1^{129}$
EPR	TEMPO–DPPC	320.5–321.1	$8.5\text{--}12^{105}$
EPR	DTBN	323	$110^{130}$
NMR	DPPC/DPPC- $d_{62}$	318–329	$0.22\text{--}0.71^{108}$
NMR	DPPC	321–326	$5.5\text{--}9^{109}$
NMR	DPPC	323	$0.54^{119}$
NMR	DPPC	318	$30^{111}$
NMR	DPPC- $d_{75}$	326	$12.2^{114}$
NMR	DPPC	323	$8.8^{110}$
NMR	DPPC- $d_8^e$	328	$14^{115}$
NMR	DPPC	325	$15.1^{131}$
NMR	DPPC	323	$14^{117}$
neutron spectroscopy			
IQENS	DPPC/DPPC- $d_{62}$	$>314.4$	$18^{100}$
IQENS	DPPC/DPPC- $d_{62}$	336	$460^{101}$
IQENS	DPPC/DPPC- $d_{62}$	333	$9.7^{102}$

<sup>a</sup>The data are presented in a chronological order for each type of method. <sup>b</sup>EPR, Electron Paramagnetic Resonance; FCS, Fluorescence Correlation Spectroscopy; FRAP, Fluorescence Recovery After Photobleaching; IQENS, Incoherent Quasi-Elastic Neutron Scattering; NMR, Nuclear Magnetic Resonance. <sup>c</sup>APE,  $N\text{--}[(\text{anthracen-9-yl})\text{-carbonyl}]\text{phosphatidylethanolamine}$ ; ASL (androstane spin label), 4',4'-dimethyl-spiro[5 $\alpha$ -androstane-17 $\beta$ -ol-3,2'-oxazolidine]-3'-oxyl; diOC<sub>18</sub>(3), 3,3'-dioctadecyloxycarbocyanine; DPPC- $d_{62}$ , 1,2-di-(palmitoyl- $d_{31}$ )-sn-glycero-3-phosphocholine; DPPC- $d_{75}$ , 1,2-di-(palmitoyl- $d_{31}$ )-sn-glycero-3-phospho(choline- $d_{13}$ ); DTBN, di-*t*-butyl-nitroxyl; NBD-DPPE,  $N\text{--}(7\text{-nitro-2,1,3-benzoxadiazol-4-yl})\text{-1,2-dipalmitoyl-sn-glycero-3-phosphoethanolamine}$ ; NBD-PC(16:0/12:0),  $N\text{--}(7\text{-nitro-2,1,3-benzoxadiazol-4-yl})\text{-2-lauroyl-1-palmitoyl-sn-glycero-3-phosphocholine}$ ; PDA, 10-(pyren-1-yl)decanoic acid; PPDPC; 1-palmitoyl-2-[10-(pyren-1-yl)decanoyl]-sn-glycero-3-phosphocholine; Rhodamine Red-X DHPE,  $N\text{--}(\text{Rhodamine Red-X})\text{-1,2-dihexadecanoyl-sn-glycero-3-phosphoethanolamine}$ ; TEMPO–DPPC,  $N,N\text{-dimethyl-}N\text{--}(2,2,6,6\text{-tetramethylpiperidin-1-oxyl-4-yl})\text{-1,2-dipalmitoyl-sn-glycero-3-phosphoethanolamine}$ . <sup>d</sup>The sample was incubated at 333 K prior to FCS measurement. <sup>e</sup>The palmitoyl chains were selectively deuterated at unspecified positions.<sup>115</sup>

the lateral diffusion coefficient that is measured is not that of the lipids in the bilayer but that of the foreign probes inserted into the bilayer. Given that these labels can be bulky, rigid, and/or reactive (as in excimer fluorescence methods), they are likely



to significantly perturb the dynamics of lipids in the bilayer.<sup>123–125</sup> Furthermore, the discrepancy between the simulations and experiment could also stem from a dependency of the diffusion coefficient on system size. Simulations<sup>68,126</sup> have highlighted for example that lipids may show collective diffusion on length scales ranging from 2.5 nm<sup>126</sup> to several tens of nanometers.<sup>68</sup> Given that the lateral size of the system in our simulations is relatively small (typically about 6.4 nm × 6.4 nm), it is very probable that  $D_{xy}$  is underestimated.

#### 4. CONCLUSION

In order to ensure the reliability of the molecular dynamics simulation of lipid bilayers, it is essential that force fields be validated against a wide range of properties measured experimentally. In this study, we have compared the accuracy and the reliability of three united-atom force fields employed in the GROMOS community to model a fluid-phase DPPC bilayer: the GROMOS S4A7 force field,<sup>28</sup> the GROMOS S3A6-derived parameters proposed by Kukol,<sup>27</sup> and the widely used modification of the Berger parameters.<sup>48</sup> We have shown that the overall structure of the bilayer (area per lipid, electron density profiles, bilayer thicknesses, and ordering of the palmitoyl chains) obtained using each of the three parameter sets is similar and within the uncertainty of the available experimental data. However, there are clear differences in the ordering of the glycerol backbone, the choline headgroup, and the orientation of the headgroup dipole between the parameter sets. Of the three parameter sets examined, the GROMOS S4A7 force field is not only the most compatible with the remainder of the GROMOS force field but also best reproduces the ordering of both the choline and glycerol moieties. In contrast, the Kukol and Berger/Anézo parameter sets show some features characteristic of a liquid-ordered phase. This is most pronounced in the case of the Kukol parameters. Importantly, it was shown that the effect of small changes in the force-field parameters was more significant than the treatment of the long-range electrostatic interactions using a reaction-field correction or PME. The lateral diffusion of the lipids in the plane of the bilayer was also examined. Although it is often calculated to validate simulations, the degree of uncertainty in the experimental measurements is such that it is not a reliable measure of quality, especially as the lateral diffusion of lipids is also highly sensitive to the simulation conditions. Other families of force fields such as CHARMM (CHARMM36<sup>15</sup>), AMBER (GAFF<sup>17,18</sup>), and OPLS<sup>20</sup> have also been recently revised in order to improve their ability to simulate fluid lipid bilayers. Whereas the method for the validation of CHARMM36 has included different types of phospholipids tested against a broad range of properties, in some other cases, the validation of force fields has been based on a small range of structural properties (for example, the area per lipid, the electron density profile, and the carbon–deuterium order parameter in the acyl chains), which, by themselves, are insufficient to determine if the parameters can be used to reproduce the properties of lipid bilayers under various conditions. While we cannot comment on parameters that we have not examined, this work demonstrates the suitability of the GROMOS S4A7 force field for modern simulations of lipid and lipid–nonlipid systems.

#### ■ ASSOCIATED CONTENT

##### Supporting Information

The details of the bonded and nonbonded force field parameters in GROMOS S4A7 and those used by Anézo et al.<sup>48</sup>

and the methodology for checking that the systems were at equilibrium when the simulations were analyzed are provided. This material is available free of charge via the Internet at <http://pubs.acs.org/>.

#### ■ AUTHOR INFORMATION

##### Corresponding Author

\*E-mail: d.poger@uq.edu.au.

##### Notes

The authors declare no competing financial interest.

#### ■ ACKNOWLEDGMENTS

This work was funded by the Australian Research Council (ARC). All the calculations were performed using high performance computing resources of the University of Queensland, the ARC (Linkage Infrastructure Equipment and Facilities grant LE0882357), and the National Computational Infrastructure (NCI) National Facility at the Australian National University under the Merit Allocation Scheme through the Queensland Cyber Infrastructure Foundation (QCIF) partner share scheme. We thank Alex H. de Vries for providing the parameter set used by Anézo et al. in their simulation study.

#### ■ REFERENCES

- (1) Wenk, M. R. *Nat. Rev. Drug Discovery* **2005**, *4*, 594–610.
- (2) Guschina, I. A.; Harwood, J. L. *FEBS Lett.* **2006**, *580*, 5477–5483.
- (3) Escibá, P. V.; González-Ros, J. M.; Goñi, F. M.; Kinnunen, P. K. J.; Vigh, L.; Sánchez-Magraner, L.; Fernández, A. M.; Busquets, X.; Horváth, I.; Barceló-Coblijn, G. *J. Cell. Mol. Med.* **2008**, *12*, 829–875.
- (4) Davletov, B.; Montecucco, C. *Curr. Opin. Neurobiol.* **2010**, *20*, 543–549.
- (5) van Meer, G.; Voelker, D. R.; Feigenson, G. W. *Nat. Rev. Mol. Cell Biol.* **2008**, *9*, 112–124.
- (6) Oliver, D.; Lien, C.-C.; Soom, M.; Baukrowitz, T.; Jonas, P.; Fakler, B. *Science* **2004**, *304*, 265–270.
- (7) Phillips, R.; Ursell, T.; Wiggins, P.; Sens, P. *Nature* **2009**, *459*, 379–385.
- (8) Lagane, B.; Gaibelet, G.; Meilhoc, E.; Masson, J.-M.; Cézanne, L.; Lopez, A. *J. Biol. Chem.* **2000**, *275*, 33197–33200.
- (9) Inagaki, S.; Ghirlando, R.; White, J. F.; Gvozdenovic-Jeremic, J.; Northup, J. K.; Grishammer, R. *J. Mol. Biol.* **2012**, *417*, 95–111.
- (10) Nagle, J. F.; Tristram-Nagle, S. *Biochim. Biophys. Acta* **2000**, *1469*, 159–195.
- (11) Vigh, L.; Escibá, P.; Sonnleitner, A.; Sonnleitner, M.; Piotto, S.; Maresca, B.; Horváth, I.; Harwood, J. L. *Prog. Lipid Res.* **2005**, *44*, 303–344.
- (12) Klauda, J. B.; Brooks, B. R.; MacKerell, A. D., Jr.; Venable, R. M.; Pastor, R. W. *J. Phys. Chem. B* **2005**, *109*, 5300–5311.
- (13) Sonne, J.; Jensen, M. Ø.; Hansen, F. Y.; Hemmingsen, L.; Peters, G. H. *Biophys. J.* **2007**, *92*, 4157–4167.
- (14) Högborg, C.-J.; Nikitin, A. M.; Lyubartsev, A. P. *J. Comput. Chem.* **2008**, *29*, 2359–2369.
- (15) Klauda, J. B.; Venable, R. M.; Freites, J. A.; O'Connor, J. W.; Tobias, D. J.; Mondragon-Ramirez, C.; Vorobyov, I.; MacKerell, A. D., Jr.; Pastor, R. W. *J. Phys. Chem. B* **2010**, *114*, 7830–7843.
- (16) Jämbeck, J. P. M.; Lyubartsev, A. P. *J. Phys. Chem. B* **2012**, *116*, 3164–3179.
- (17) Jójárt, B.; Martinek, T. A. *J. Comput. Chem.* **2007**, *28*, 2051–2058.
- (18) Rosso, L.; Gould, I. R. *J. Comput. Chem.* **2008**, *29*, 24–37.
- (19) Siu, S. W. I.; Vácha, R.; Jungwirth, P.; Böckmann, R. A. *J. Chem. Phys.* **2008**, *128*, 125103.
- (20) Ulmschneider, J. P.; Ulmschneider, M. B. *J. Chem. Theory Comput.* **2009**, *5*, 1803–1813.

- (21) Siu, S. W. I.; Pluhackova, K.; Böckmann, R. A. *J. Chem. Theory Comput.* **2012**, *8*, 159–1470.
- (22) Egberts, E.; Marrink, S.-J.; Berendsen, H. J. C. *Eur. Biophys. J.* **1994**, *22*, 423–436.
- (23) Chiu, S.-W.; Clark, M.; Balaji, V.; Subramaniam, S.; Scott, H. J.; Jakobsson, E. *Biophys. J.* **1995**, *69*, 1230–1245.
- (24) Berger, O.; Edholm, O.; Jähnig, F. *Biophys. J.* **1997**, *72*, 2002–2013.
- (25) Zhao, W.; Róg, T.; Gurtovenko, A. A.; Vattulainen, I.; Karttunen, M. *Biophys. J.* **2007**, *92*, 1114–1124.
- (26) Chiu, S.-W.; Pandit, S. A.; Scott, H. L.; Jakobsson, E. *J. Phys. Chem. B* **2009**, *113*, 2748–2763.
- (27) Kukol, A. *J. Chem. Theory Comput.* **2009**, *5*, 615–626.
- (28) Poger, D.; van Gunsteren, W. F.; Mark, A. E. *J. Comput. Chem.* **2010**, *30*, 117–1125.
- (29) Dománski, J.; Stansfeld, P. J.; Sansom, M. S. P.; Beckstein, O. *J. Membr. Biol.* **2010**, *236*, 255–258.
- (30) Luzzati, V.; Husson, F. *J. Cell Biol.* **1962**, *12*, 207–219.
- (31) Seddon, J. M.; Templer, R. H. In *Handbook of Biological Physics*; Lipowsky, R., Sackmann, E., Eds.; Elsevier Science B. V.: Amsterdam, 1995; Vol. 1, Chapter 3.
- (32) Poger, D.; Mark, A. E. *J. Chem. Theory Comput.* **2010**, *6*, 325–336.
- (33) van Gunsteren, W. F.; Berendsen, H. J. C. *Groningen Molecular Simulation (GROMOS) Library Manual*; BIOMOS B.V.: Nijenborgh, Groningen, The Netherlands, 1987.
- (34) van Gunsteren, W. F.; Billeter, S. R.; Eising, A. A.; Hünenberger, P. H.; Krüger, P.; Mark, A. E.; Scott, W. R. P.; Tironi, I. G. *Biomolecular Simulation: The GROMOS96 Manual and User Guide*; vdf Hochschulverlag AG an der ETH Zürich and BIOMOS B.V.: Zürich, Groningen, 1996.
- (35) Daura, X.; Mark, A. E.; van Gunsteren, W. F. *J. Comput. Chem.* **1998**, *19*, 535–547.
- (36) Schuler, L. D.; van Gunsteren, W. F. *Mol. Simul.* **2000**, *25*, 301–319.
- (37) Schuler, L. D.; Daura, X.; van Gunsteren, W. F. *J. Comput. Chem.* **2001**, *22*, 1205–1218.
- (38) Chandrasekhar, I.; Kastenholz, M.; Lins, R. D.; Oostenbrink, C.; Schuler, L. D.; Tieleman, P. D.; van Gunsteren, W. F. *Eur. Biophys. J.* **2003**, *32*, 67–77.
- (39) Lins, R. D.; Hünenberger, P. H. *J. Comput. Chem.* **2005**, *26*, 1400–1412.
- (40) Soares, T. A.; Hünenberger, P. H.; Kastenholz, M. A.; Kräutler, V.; Lenz, T.; Lins, R. D.; Oostenbrink, C.; van Gunsteren, W. F. *J. Comput. Chem.* **2005**, *26*, 725–737.
- (41) Oostenbrink, C.; Villa, A.; Mark, A. E.; van Gunsteren, W. F. *J. Comput. Chem.* **2004**, *25*, 1656–1676.
- (42) Schmid, N.; Eichenberger, A. P.; Choutko, A.; Riniker, S.; Winger, M.; Mark, A. E.; van Gunsteren, W. F. *Eur. Biophys. J.* **2011**, *40*, 843–856.
- (43) Chandrasekhar, I.; Oostenbrink, C.; van Gunsteren, W. F. *Soft Mater.* **2004**, *2*, 27–45.
- (44) Chandrasekhar, I.; Bakowies, D.; Glättli, A.; Hünenberger, P.; Pereira, C.; van Gunsteren, W. F. *Mol. Simul.* **2005**, *31*, 543–548.
- (45) Jorgensen, W. L.; Tirado-Rives, J. *J. Am. Chem. Soc.* **1988**, *110*, 1657–1666.
- (46) Prakash, P.; Sankaramakrishnan, R. *J. Comput. Chem.* **2010**, *31*, 266–277.
- (47) Piggot, T. J.; Piñeiro, Á.; Khalid, S. *J. Chem. Theory Comput.* **2012**, in press.
- (48) Anézo, C.; de Vries, A. H.; Hölte, H.-D.; Tieleman, D. P.; Marrink, S.-J. *J. Phys. Chem. B* **2003**, *107*, 9424–9433.
- (49) Patra, M.; Karttunen, M.; Hyvönen, M. T.; Falck, E.; Lindqvist, P.; Vattulainen, I. *Biophys. J.* **2003**, *84*, 3636–3645.
- (50) Patra, M.; Karttunen, M.; Hyvönen, M. T.; Falck, E.; Vattulainen, I. *J. Phys. Chem. B* **2004**, *108*, 4485–4494.
- (51) Tieleman, D. P.; Berendsen, H. J. C. *J. Chem. Phys.* **1996**, *105*, 4871–4880.
- (52) Castro-Román, F.; Benz, R. W.; White, S. H.; Tobias, D. J. *J. Phys. Chem. B* **2006**, *110*, 24157–24164.
- (53) Darden, T.; York, D.; Pedersen, L. *J. Chem. Phys.* **1993**, *98*, 10089–10092.
- (54) Essmann, U.; Perera, L.; Berkowitz, M. L.; Darden, T.; Lee, H.; Pedersen, L. G. *J. Chem. Phys.* **1995**, *103*, 8577–8593.
- (55) Tironi, I. G.; Sperb, R.; Smith, P. E.; van Gunsteren, W. F. *J. Chem. Phys.* **1995**, *102*, 5451–5459.
- (56) Nagle, J. F.; Zhang, R.; Tristram-Nagle, S.; Sun, W.; Petrache, H. I.; Suter, R. M. *Biophys. J.* **1996**, *70*, 1419–1431.
- (57) Malde, A. K.; Zuo, L.; Breeze, M.; Stroet, M.; Poger, D.; Nair, P. C.; Oostenbrink, C.; Mark, A. E. *J. Chem. Theory Comput.* **2011**, *7*, 4026–4037.
- (58) Ryckaert, J.-P.; Bellemans, A. *Chem. Phys. Lett.* **1975**, *30*, 123–128.
- (59) Ryckaert, J.-P.; Bellemans, A. *Faraday Discuss. Chem. Soc.* **1978**, *66*, 95–106.
- (60) van der Spoel, D.; Lindahl, E.; Hess, B.; Groenhof, G.; Mark, A. E.; Berendsen, H. J. C. *J. Comput. Chem.* **2005**, *26*, 1701–1718.
- (61) Berendsen, H. J. C.; Postma, J. P. M.; van Gunsteren, W. F.; DiNola, A.; Haak, J. R. *J. Chem. Phys.* **1984**, *81*, 3684–3690.
- (62) Mabrey, S.; Sturtevant, J. M. *Proc. Natl. Acad. Sci. U. S. A.* **1976**, *73*, 3862–3866.
- (63) Huang, C. H.; Lapidus, J. R.; Levin, I. W. *J. Am. Chem. Soc.* **1982**, *104*, 5926–5930.
- (64) Hess, B.; Bekker, H.; Berendsen, H. J. C.; Fraaije, J. G. E. M. *J. Comput. Chem.* **1997**, *18*, 1463–1472.
- (65) Berendsen, H. J. C.; Postma, J. P. M.; van Gunsteren, W. F.; Hermans, J. In *Intermolecular Forces*; Reidel: Dordrecht, The Netherlands, 1981; pp 331–342.
- (66) Miyamoto, S.; Kollman, P. A. *J. Comput. Chem.* **1992**, *13*, 952–962.
- (67) Feenstra, K.; Hess, B.; Berendsen, H. J. C. *J. Comput. Chem.* **1999**, *20*, 786–798.
- (68) Falck, E.; Róg, T.; Karttunen, M.; Vattulainen, I. *J. Am. Chem. Soc.* **2008**, *130*, 44–45.
- (69) Heinz, T. N.; van Gunsteren, W. F.; Hünenberger, P. H. *J. Chem. Phys.* **2001**, *115*, 1125–1136.
- (70) Kučerka, N.; Nagle, J. F.; Sachs, J. N.; Feller, S. E.; Pencer, J.; Jackson, A.; Katsaras, J. *Biophys. J.* **2008**, *95*, 2356–2367.
- (71) Petrache, H. I.; Dodd, S. W.; Brown, M. F. *Biophys. J.* **2000**, *79*, 3172–3192.
- (72) Kučerka, N.; Tristram-Nagle, S.; Nagle, J. F. *Biophys. J.* **2006**, *90*, L83–L85.
- (73) Wiener, M. C.; Suter, R. M.; Nagle, J. F. *Biophys. J.* **1989**, *55*, 315–325.
- (74) Lis, L. J.; McAlister, M.; Fuller, N.; Rand, R. P.; Parsegian, V. A. *Biophys. J.* **1982**, *37*, 657–665.
- (75) Douliez, J.-P.; Léonard, A.; Dufourc, E. J. *Biophys. J.* **1995**, *68*, 1727–1739.
- (76) Seelig, A.; Seelig, J. *Biochim. Biophys. Acta* **1975**, *406*, 1–5.
- (77) Seelig, J.; Seelig, A. *Q. Rev. Biophys.* **1980**, *13*, 19–61.
- (78) Davis, J. H. *Biochim. Biophys. Acta* **1983**, *737*, 117–171.
- (79) Bonev, B. B.; Morrow, M. R. *Biophys. J.* **1995**, *69*, 518–523.
- (80) Seelig, J.; Gally, H.-U.; Wohlgemuth, R. *Biochim. Biophys. Acta* **1977**, *467*, 109–119.
- (81) Akutsu, H.; Seelig, J. *Biochemistry* **1981**, *20*, 7366–7373.
- (82) Gally, H.-U.; Niederberger, W.; Seelig, J. *Biochemistry* **1975**, *14*, 3647–3652.
- (83) Macdonald, P. M.; Leisen, J.; Marassi, F. M. *Biochemistry* **1991**, *30*, 3558–3566.
- (84) Scherer, P. G.; Seelig, A. *Biochemistry* **1989**, *28*, 7720–7728.
- (85) Gally, H. U.; Pluschke, G.; Overath, P.; Seelig, J. *Biochemistry* **1981**, *20*, 1826–1831.
- (86) Büldt, G.; Gally, H. U.; Seelig, A.; Seelig, J.; Zaccari, G. *Nature* **1978**, *271*, 182–184.
- (87) Lindahl, E.; Edholm, O. *J. Chem. Phys.* **2001**, *115*, 4938–4950.
- (88) Bonvin, A. M. J. J.; Mark, A. E.; van Gunsteren, W. F. *Comput. Phys. Commun.* **2000**, *128*, 550–557.

- (89) Vaz, W. L. C.; Clegg, R. M.; Hallmann, D. *Biochemistry* **1985**, *24*, 781–786.
- (90) Scomparin, C.; Lecuyer, S.; Ferreira, M.; Charitat, T.; Tinland, B. *Eur. Phys. J. E: Soft Matter Biol. Phys.* **2009**, *28*, 211–220.
- (91) Kušba, J.; Li, L.; Gryczynski, I.; G., P.; M., J.; Lakowicz, J. R. *Biophys. J.* **2002**, *82*, 1358–1372.
- (92) Galla, H.-J.; Hartmann, W.; Theilen, U.; Sackmann, E. *J. Membr. Biol.* **1979**, *48*, 215–236.
- (93) Merkel, R.; Sackmann, E. *J. Phys. Chem.* **1994**, *98*, 4428–4442.
- (94) Korlach, J.; Schwille, P.; Webb, W. W.; Feigenson, G. W. *Proc. Natl. Acad. Sci. U. S. A.* **1999**, *96*, 8461–8466.
- (95) Benda, A.; Beneš, M.; Mareček, V.; Lhotský, A.; Hermens, W. T.; Hof, M. *Langmuir* **2003**, *19*, 4120–4126.
- (96) Heinemann, F.; Schwille, P. *ChemPhysChem* **2011**, *12*, 2568–2571.
- (97) Fujiwara, T.; Ritchie, K.; Murakoshi, H.; Jacobson, K.; Kusu, J. *Cell Biol.* **2002**, *157*, 1071–1082.
- (98) Martin, D. S.; Forstner, M. B.; Käs, J. A. *Biophys. J.* **2002**, *83*, 2109–2117.
- (99) Dietrich, C.; Merkel, R.; Tampé, R. *Biophys. J.* **1997**, *72*, 1701–1710.
- (100) Pfeiffer, W.; Henkel, T.; Sackmann, E.; Knoll, W.; Richter, D. *Europhys. Lett.* **1989**, *8*, 201–206.
- (101) Tabony, J.; Perly, B. *Biochim. Biophys. Acta* **1990**, *1063*, 67–72.
- (102) König, S.; Pfeiffer, W.; Bayerl, T.; Richter, D.; Sackmann, E. *J. Phys. II* **1992**, *2*, 1589–1615.
- (103) Swenson, J.; Kargl, F.; Berntsen, P.; Svanberg, C. J. *Chem. Phys.* **2008**, *129*, 045101.
- (104) Devaux, P.; McConnell, H. J. *Am. Chem. Soc.* **1972**, *94*, 4475–4481.
- (105) Sheats, J. R.; McConnell, H. M. *Proc. Natl. Acad. Sci. U. S. A.* **1978**, *75*, 4661–4663.
- (106) Haibel, A.; Nimtz, G.; Pelster, R.; Jaggi, R. *Phys. Rev. E* **1998**, *57*, 4838–4841.
- (107) Galera-Cortés, E.; de Dios Solier, J.; Estelrich, J.; Hidalgó-Álvarez, R. *Langmuir* **2010**, *26*, 2665–2670.
- (108) Fisher, R. W.; James, T. L. *Biochemistry* **1978**, *17*, 1177–1183.
- (109) Kuo, A.-L.; Wade, C. G. *Biochemistry* **1979**, *18*, 2300–2308.
- (110) Picard, F.; Paquet, M.-J.; Dufourc, E. J.; Auger, M. *Biophys. J.* **1998**, *74*, 857–868.
- (111) Fenske, D. B.; Jarrell, H. C. *Biophys. J.* **1991**, *59*, 55–69.
- (112) Dolainsky, C.; Unger, M.; Bloom, M.; Bayerl, T. M. *Phys. Rev. E* **1995**, *51*, 4743–4750.
- (113) Heaton, N. J.; Althoff, G.; Kothe, G. *J. Phys. Chem.* **1996**, *100*, 4944–4953.
- (114) Karakatsanis, P.; Bayerl, T. M. *Phys. Rev. E* **1996**, *54*, 1785–1790.
- (115) Hetzer, M.; Heinz, S.; Grage, S.; Bayerl, T. M. *Langmuir* **1998**, *14*, 982–984.
- (116) Orädd, G.; Westerman, P. W.; Lindblom, G. *Biophys. J.* **2005**, *89*, 315–320.
- (117) Lindblom, G.; Orädd, G.; Filippov, A. *Chem. Phys. Lipids* **2006**, *141*, 179–184.
- (118) Daems, D.; van den Zegel, M.; Boens, N.; De Schryver, F. C. *Eur. Biophys. J.* **1985**, *12*, 97–105.
- (119) Lee, B.-S.; Mabry, S. A.; Jonas, A.; Jonas, J. *Chem. Phys. Lipids* **1995**, *78*, 103–117.
- (120) Filippov, A.; Orädd, G.; Lindblom, G. *Langmuir* **2003**, *19*, 6397–6400.
- (121) Sezgin, E.; Schwille, P. *Cold Spring Harbor Perspect. Biol.* **2011**, *3*, a009803.
- (122) Vaz, W. L. C.; Almeida, P. F. *Biophys. J.* **1991**, *60*, 1553–1554.
- (123) Filipe, H. A. L.; João Moreno, M.; Loura, L. M. S. *J. Phys. Chem. B* **2011**, *115*, 10109–10119.
- (124) Muddana, H. S.; Gullapalli, R. R.; Manias, E.; Butler, P. J. *Phys. Chem. Chem. Phys.* **2011**, *13*, 1368–1378.
- (125) Skaug, M. J.; Longo, M. L.; Faller, R. J. *J. Phys. Chem. B* **2011**, *115*, 8500–8505.
- (126) Roark, M.; Feller, S. E. *J. Phys. Chem. B* **2009**, *113*, 13229–132234.
- (127) Razi Naqvi, K.; Behr, J.-P.; Chapman, D. *Chem. Phys. Lett.* **1974**, *26*, 440–444.
- (128) Wu, E.-S.; Jacobson, K.; Papahadjopoulos, D. *Biochemistry* **1977**, *16*, 3936–3941.
- (129) Träuble, H.; Sackmann, E. *J. Am. Chem. Soc.* **1972**, *94*, 4499–4510.
- (130) Dix, J. A.; Diamond, J. A.; Kivelson, D. K. *Proc. Natl. Acad. Sci. U. S. A.* **1974**, *71*, 474–478.
- (131) Scheidt, H. A.; Huster, D.; Gawrisch, K. *Biophys. J.* **2005**, *89*, 2504–2512.